Inorganic Chemistry

Article

pubs.acs.org/IC

Complete Series of Chiral Paramagnetic Molecular Conductors Based on Tetramethyl-bis(ethylenedithio)-tetrathiafulvalene (TM-BEDT-TTF) and Chloranilate-Bridged Heterobimetallic Honeycomb Layers

Matteo Atzori,[†,‡] Flavia Pop,[‡] Pascale Auban-Senzier,[∥] Rodolphe Clérac,[#,§] Enric Canadell,[◊] Maria Laura Mercuri,*[,†] and Narcis Avarvari*[,‡]

[†]Dipartimento di Scienze Chimiche e Geologiche, Università degli Studi di Cagliari, S.S. 554 − Bivio per Sestu − I09042 Monserrato (Cagliari), Italy

[‡]Laboratoire MOLTECH-Anjou UMR 6200, UFR Sciences, CNRS, Université d'Angers, Bât. K, 2 Bd. Lavoisier, 49045 Angers, France

[∥]Laboratoire de Physique des Solides, UMR 8502, Bât. 510, CNRS-Université Paris-Sud, 91405 Orsay, France

[#]CNRS, CRPP, UPR 8641, F-33600 Pessac, France

[§]Univ. Bordeaux, CRPP, UPR 8641, F-33600 Pessac, France

[◊]Institut de Ciència de Materials de Barcelona (CSIC), Campus de la UAB, E-08193 Bellaterra, Spain

Supporting Information

ABSTRACT: Electrocrystallization of enantiopure (*S,S,S,S*)- and (*R,R,R,R*)-tetramethyl-bis(ethylenedithio)-tetrathiafulvalene (TM-BEDT-TTF) donors, as well as the racemic mixture, in the presence of potassium cations and the tris(chloranilato)-ferrate(III) $[Fe(Cl_2An)_3]^{3-}$ paramagnetic anion afforded a complete series of chiral magnetic molecular conductors formulated as *β*-[(*S,S,S,S*)-TM-BEDT-TTF]$_3$PPh$_4$[K^{I}Fe^{III}(Cl$_2$An)$_3$]·3H$_2$O (**1**), *β*-[(*R,R,R,R*)-TM-BEDT-TTF]$_3$PPh$_4$[K^{I}Fe^{III}(Cl$_2$An)$_3$]·3H$_2$O (**2**), and *β*-[(*rac*)-TM-BEDT-TTF]$_3$PPh$_4$[K^{I}Fe^{III}(Cl$_2$An)$_3$]·3H$_2$O (**3**). Compounds **1**−**3** are isostructural and crystallize in triclinic space groups (*P*1 for **1** and **2**, *P*−1 for **3**) showing a segregated organic−inorganic crystal structure, where anionic honeycomb layers obtained by self-assembling of the Λ and Δ enantiomers of the paramagnetic complex with potassium cations alternate with organic layers where the chiral donors are arranged in the *β* packing motif. Compounds **1**−**3** show a molecular packing strongly influenced by the topology of the inorganic layers and behave as molecular semiconductors with room-temperature conductivity values of ca. 3×10^{-4} S cm^{-1}. The magnetic properties are dominated by the paramagnetic $S = 5/2$ $[Fe(Cl_2An)_3]^{3-}$ anions whose high-spin character is confirmed by magnetic susceptibility measurements. The correlation between crystal structure and conducting behavior has been studied by means of tight-binding band structure calculations which support the observed conducting properties.

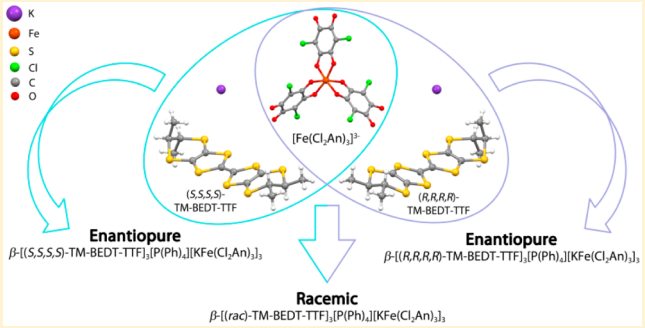

INTRODUCTION

The introduction of chirality in the field of tetrathiafulvalene (TTF) based molecular conductors represents one of the most recent advances[1] in the search for multifunctional molecular materials where properties such as charge transport, magnetism, spin crossover, chirality, and so on, coexist or interplay in the same material.[2] One of the milestones in this field is the first observation of the electrical magneto-chiral anisotropy (eMChA) effect in a bulk crystalline chiral conductor,[3] as a synergy between chirality and conductivity.[4] However, the combination of chirality with electroactivity in chiral TTF precursors afforded several other recent important results such as the following: (i) the modulation of the structural disorder in the solid state and hence a difference in conductivity between the enantiopure and racemic forms, as observed in conducting salts based on ethylenedithio-TTF-oxazolines (EDT-TTF-Ox);[5] (ii) the tuning of the chiroptical properties through electrochemical or chemical oxidation, as observed, for example, in TTF-allenes[6] or TTF-helicenes;[7] (iii) the control of the supramolecular chirality in electroactive helical aggregates;[8] (iv) the induction of different packing patterns and crystalline space groups in mixed valence salts of dimethyl-ethylenedithio-TTF (DM-EDT-TTF) showing semiconducting (enantiopure forms) or metallic (racemic form) behavior;[9] or (v) the access to electroactive chiral ligands.[10] Although the first example of an enantiopure TTF derivative, namely, the tetramethyl-bis(ethylenedithio)-tetrathiafulvalene (TM-BEDT-TTF) (see

Received: February 3, 2015
Published: March 24, 2015

DOI: 10.1021/acs.inorgchem.5b00261
Inorg. Chem. 2015, 54, 3643−3653

Scheme 1), was described almost 30 years ago as the (*S,S,S,S*) enantiomer,[11] the number of TM-BEDT-TTF-based conducting radical cation salts is rather limited. They range from the semiconducting salts $[TM\text{-}BEDT\text{-}TTF]_2XF_6$ (X = As, Sb)[12] or $[TM\text{-}BEDT\text{-}TTF]I_3$,[13] as complete series of both enantiomers and racemic forms, to the ferromagnetic metal $[TM\text{-}BEDT\text{-}TTF]_x[MnCr(ox)_3]$, described only as the (*S,S,S,S*) enantiomer.[14] With respect to this last system, the use of magnetic counterions is particularly interesting because they provide an additional property to the system, as it was largely explored, for example, in the case of the metal-oxalates $[M(ox)_3]^{3-}$ (M = Fe^{3+}, Cr^{3+}, Ga^{3+}, ox = oxalate),[15] present as Δ and Λ enantiomers in radical cation salts based on the bis(ethylenedithio)-tetrathiafulvalene (BEDT-TTF) donor. Other paramagnetic chiral anions, such as $[Fe(croc)_3]^{3-}$ (croc = croconate)[16] or $[Cr(2,2'\text{-bipy})(ox)_2]^-$ (bipy = bipyridine),[17] have been scarcely used up to now. However, in all these magnetic conductors, the tris-chelated anions were present as racemic mixtures, excepting a case where the Δ enantiomer of $[Cr(ox)_3]^{3-}$ crystallized preferentially in the presence of (*R*)-carvone as chiral cosolvent in the electrocrystallization experiments.[18] As far as the π−*d* systems are concerned (i.e., systems where delocalized π−electrons of the organic donor are combined with localized *d*−electrons of magnetic counterions), the number of conducting systems based on enantiopure TTF precursors is even scarcer. One example concerns the above-mentioned ferromagnetic metal $[TM\text{-}BEDT\text{-}TTF]_x[MnCr(ox)_3]$,[14] while a more recent one is represented by the semiconducting paramagnetic salts $[DM\text{-}BEDT\text{-}TTF]_4[ReCl_6]$ (DM-BEDT-TTF = dimethyl-bis(ethylenedithio)-tetrathiafulvalene).[19] In this respect, anilate-based metal complexes, namely, metal complexes of 3,6-disubstituted-2,5-dihydroxy-1,4-benzoquinones, formulated as $[M^{III}(X_2An)_3]^{3-}$ (M^{III} = Fe, Cr; X = H,[20] Cl, Br, I;[21] An = anilate = $C_6O_4^{2-}$), are very interesting molecular building blocks to be used as paramagnetic components for obtaining conducting radical cation salts,[22] also because they offer the opportunity to provide magnetic exchange coupling through the anilate bridge, as observed in layered heterobimetallic compounds showing ferrimagnetic ordering and tunable ordering temperatures.[23] Moreover, the anilate ligands can be conveniently functionalized with redox active moieties such as thiophenes.[24]

Scheme 1. Molecular Structures for the Complex Anion $[Fe(Cl_2An)_3]^{3-}$ and the TM-BEDT-TTF Chiral Donor

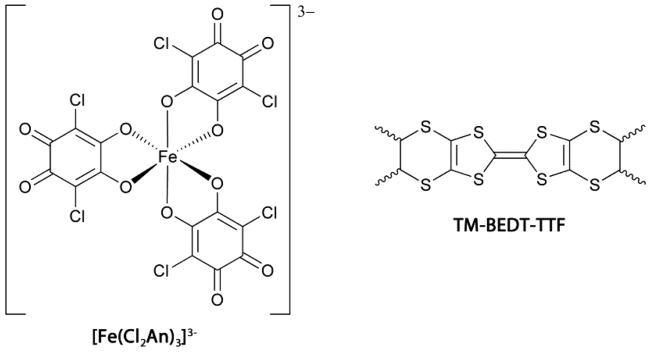

Thus, with the aim to explore the potential of both anilate-based molecular building blocks and chiral TTF derivatives in the construction of π−*d* multifunctional materials, the tris(chloranilato)ferrate(III) $[Fe(Cl_2An)_3]^{3-}$ complex anion (Scheme 1) has been combined, in the presence of potassium cations, with the TM-BEDT-TTF organic donor as (*S,S,S,S*) and (*R,R,R,R*) enantiopure forms or as racemic mixture (*rac*).

We describe herein a complete series of chiral hybrid systems, formulated as $[TM\text{-}BEDT\text{-}TTF]_3PPh_4[K^IFe^{III}(Cl_2An)_3]\cdot 3H_2O$, representing the first family of chiral radical cation salts with chloranilate-bridged heterobimetallic honeycomb layers. Their synthesis, crystal structures, physical properties, and tight-binding band structure calculations are thoroughly discussed.

RESULTS AND DISCUSSION

Synthesis. Electrocrystallization of enantiopure (*S,S,S,S*)-, (*R,R,R,R*)- or (*rac*)-TM-BEDT-TTF, the latter obtained by mixing equimolar amounts of pure enantiomers, in the presence of potassium cations and the tris(chloranilato)ferrate(III) $[Fe(Cl_2An)_3]^{3-}$ paramagnetic chiral anion (Scheme 1), afforded a complete series of radical cation salts formulated as β-[(*S,S,S,S*)-TM-BEDT-TTF]$_3PPh_4[K^IFe^{III}(Cl_2An)_3]\cdot 3H_2O$ (**1**), β-[(*R,R,R,R*)-TM-BEDT-TTF]$_3PPh_4[K^IFe^{III}(Cl_2An)_3]\cdot 3H_2O$ (**2**) and β-[(*rac*)-TM-BEDT-TTF]$_3PPh_4[K^IFe^{III}(Cl_2An)_3]\cdot 3H_2O$ (**3**).

The successful synthetic strategy for obtaining these systems consists in combining the so-called "complex as ligand" approach with a classical electrocrystallization experiment. More specifically, the octahedral complex tris(chloranilato)ferrate(III) $[Fe(Cl_2An)_3]^{3-}$ was used as ligand toward potassium cations, thus affording, in a first step, dianionic heterobimetallic layers, which, subsequently, has combined with oxidized donors and tetraphenylphosphonium cations to provide a segregated organic−inorganic solid state structure.

Crystal Structures. The three hybrid systems **1**−**3** are isostructural, excepting the space group, and present a crystal structure formed by alternating heterobimetallic chloranilate-based honeycomb double-layers and layers of TM-BEDT-TTF radical cations. Compounds **1** and **2** crystallize in the

Table 1. Fe−O Bond Distances (Å) for the Iron Complex Subunit in Compounds 1−3 Compared with the Reported Values for the Isolated $[Fe(Cl_2An)_3]^{3-}$ Anion as PPh_4^+ Salt[21] and for Its BEDT-TTF Radical Cation Salts[22]

bonds	1	2	3	$[BEDT\text{-}TTF]_3[Fe(Cl_2An)_3]$	δ-$[BEDT\text{-}TTF]_5[Fe(Cl_2An)_3]$	α‴-$[BEDT\text{-}TTF]_{18}[Fe(Cl_2An)_3]_3$	$[PPh_4]_3[Fe(Cl_2An)_3]$
Fe−O(11)	2.025(8)	2.007(6)	2.009(6)	1.996(5)	2.008(6)	2.020(6)	2.002(6)
Fe−O(21)	2.002(8)	2.045(5)	2.020(6)	2.002(4)	2.022(6)	2.028(6)	2.008(6)
Fe−O(12)	1.994(8)	1.988(5)	2.017(6)	2.018(4)	2.019(5)	1.994(7)	2.001(6)
Fe−O(22)	2.001(7)	2.018(5)	1.999(6)	1.998(4)	1.999(6)	2.028(6)	2.017(6)
Fe−O(13)	2.019(8)	2.030(5)	2.010(6)	2.026(4)	2.039(6)	2.018(6)	2.013(6)
Fe−O(23)	1.987(8)	2.000(5)	2.041(6)	2.037(4)	2.014(6)	1.989(7)	1.999(6)
average Fe−O	2.005(8)	2.014(5)	2.016(6)	2.013(4)	2.017(6)	2.013(6)	2.007(6)

DOI: 10.1021/acs.inorgchem.5b00261
Inorg. Chem. 2015, 54, 3643−3653

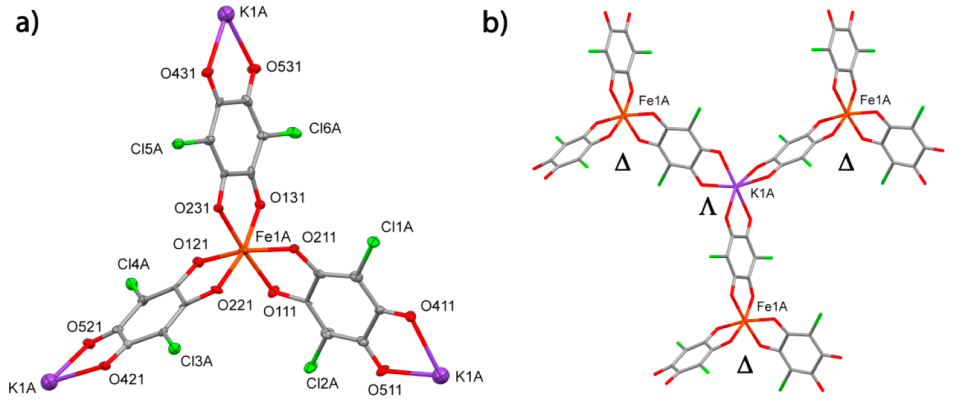

Figure 1. (a) ORTEP drawing for the tris(chloranilato)ferrate(III) unit (Δ enantiomer) connected to three K^+ cations for **2** (thermal ellipsoids at the 30% probability level); (b) Schematic view of the K^+ cation (Λ enantiomer) coordinated by three $[Fe(Cl_2An)_3]^{3-}$ units.

noncentrosymmetric triclinic space group *P1* with six crystallographically independent TM-BEDT-TTF chiral donors ((*S,S,S,S*) configuration for **1** and (*R,R,R,R*) configuration for **2**), two $[K^IFe^{III}(Cl_2An)_3]^{2-}$ units, whose metal centers exhibit opposite stereochemical configuration ($[\Lambda\text{-}K^I\Delta\text{-}Fe^{III}(Cl_2An)_3]^{2-}$ and $[\Delta\text{-}K^I\Lambda\text{-}Fe^{III}(Cl_2An)_3]^{2-}$), and two charge-compensating PPh_4^+ cations in the unit cell. Compound **3** crystallizes in the centrosymmetric triclinic space group *P−1* and contains half of the content of **1** and **2** in the asymmetric unit, since the stereochemically opposite content is generated by the inversion center.

In each system the iron complexes retain the octahedral coordination geometry of the starting building block, with the Fe(III) ion surrounded by six oxygen atoms of three chloranilate chelating ligands. The iron−oxygen bond distances in compounds **1**−**3** vary in the 1.987(8)−2.030(5) Å range and are close to those observed for the $[PPh_4]_3[Fe(Cl_2An)_3]$ precursor[21] and for its BEDT-TTF radical cation salts[22] (Table 1). These data are in accordance with a high spin character of the Fe(III) ions (*vide infra*).

The six peripheral oxygen atoms of each $[Fe(Cl_2An)_3]^{3-}$ unit act as additional 1,2-bidentate coordinating sites toward three potassium cations (Figure 1a), so that each K(I) center is coordinated by three different $[Fe(Cl_2An)_3]^{3-}$ units in a slightly distorted octahedral coordination geometry (Figure 1b).

The potassium−oxygen bond distances in compounds **1**−**3**, ranging from 2.259(8) to 2.382(9) Å (Table 2), are very short

Table 2. K−O Bond Distances (Å) for Compounds 1−3

bonds	1	2	3
K−O(41)	2.382(9)	2.356(6)	2.338(7)
K−O(51)	2.364(9)	2.346(7)	2.357(7)
K−O(42)	2.408(9)	2.311(7)	2.303(7)
K−O(52)	2.259(8)	2.367(6)	2.392(8)
K−O(43)	2.394(9)	2.372(6)	2.332(7)
K−O(53)	2.347(9)	2.375(7)	2.378(7)
average K−O	2.359(9)	2.354(7)	2.350(7)

if compared to the sum of the K and O ionic radii (ca. 2.9 Å), or the already observed $K^+\cdots O$ interactions involving potassium cations and mononuclear chloranilate-based complexes (shortest distance of ca. 2.9 Å in a secondary interaction)[25] or hydrogen chloranilate (HCl_2An^-) (shortest distance of ca. 2.7 Å in a tricapped trigonal prismatic geometry).[26]

It is noteworthy that an octahedral coordination geometry exhibited by an alkali metal ion having anilates as ligands was never observed, whereas coordination geometries with higher coordination numbers are already known.[27] The C−O bond distances of the ligand are influenced by the coordination to the metal centers. The oxygen atoms coordinated to the Fe(III) have C−O distances on average 0.05 Å longer than those of the oxygen atoms coordinated to the K(I), which show a higher double bond character (Table S1).

The iron complexes combined with potassium cations in the electrocrystallization experiment generate anionic layers formulated as $[K^IFe^{III}(Cl_2An)_3]^{2-}$, showing the hexagonal honeycomb topology[28] where the Fe(III) and K(I) ions, connected through the 1,2-bis-bidentate chloranilate ligand, alternate on the vertexes of an hexagon (Figure 2), as already observed in analogous heterobimetallic systems.[23]

It should be highlighted that, in each layer, all the $[Fe(Cl_2An)_3]^{3-}$ units have the same stereochemical configuration and, consequently, the K(I) centers have the opposite one (e.g., $[\Delta\text{-}Fe^{III}\Lambda\text{-}K^I(Cl_2An)_3]^{2-}$ or *vice versa*) (Figure 1b and Figure S1).

Another peculiarity in the structure of these salts is the double-layer association of the heterobimetallic coordination polymers. This is likely due to the establishment of two predominant intermolecular interactions: Cl···Cl interactions lower than the sum of the van der Waals radii (3.50 Å) between the chlorine atoms on the ligands of adjacent layers, and $\pi-\pi$ stacking interactions between the chloranilate ligands and the phenyl rings of the PPh_4^+ molecules that are present between the layers as charge-compensating cations (Figure 3 and Figure S2).

It should be highlighted that the Cl···Cl interactions (Cl(5A)···Cl(2B) 3.42 Å, Cl(1A)···Cl(5B) 3.42 Å) directly connect two adjacent layers, whereas those mediated by the PPh_4^+ cations involve multiple $\pi-\pi$ stacking interactions either between the chloranilate ligands and the phenyl rings (L31···CH2 4.00 Å, L32···CG1 3.85 Å) or between phenyl rings of adjacent PPh_4^+ molecules (CH1···CG2 4.54 Å, CH4···CG3 6.24 Å), as already observed in other supramolecular architectures involving tris(anilato)metalate(III) complexes and PPh_4^+ cations.[20] These interactions force the anionic layers in an alternate disposition (Figure S3) instead of an eclipsed one.[23]

In the crystal structure of compounds **1**−**3**, these inorganic layers alternate with cationic layers formed by the chiral donor

DOI: 10.1021/acs.inorgchem.5b00261
Inorg. Chem. 2015, 54, 3643−3653

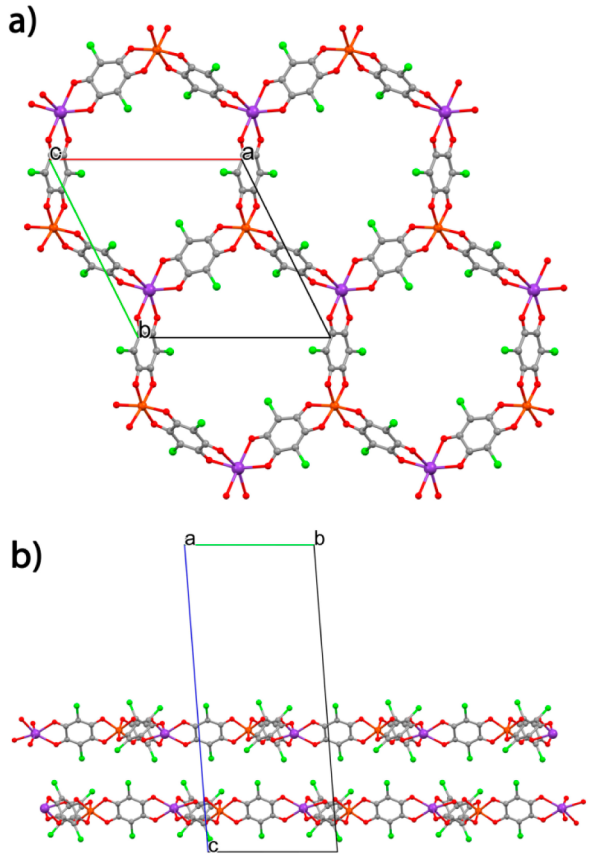

Figure 2. (a) Top view of the anionic layers parallel to the *ab* plane showing the connection and alternation of Fe(III) and K(I) ions through the chloranilate ligand; (b) Side view of the anionic layers.

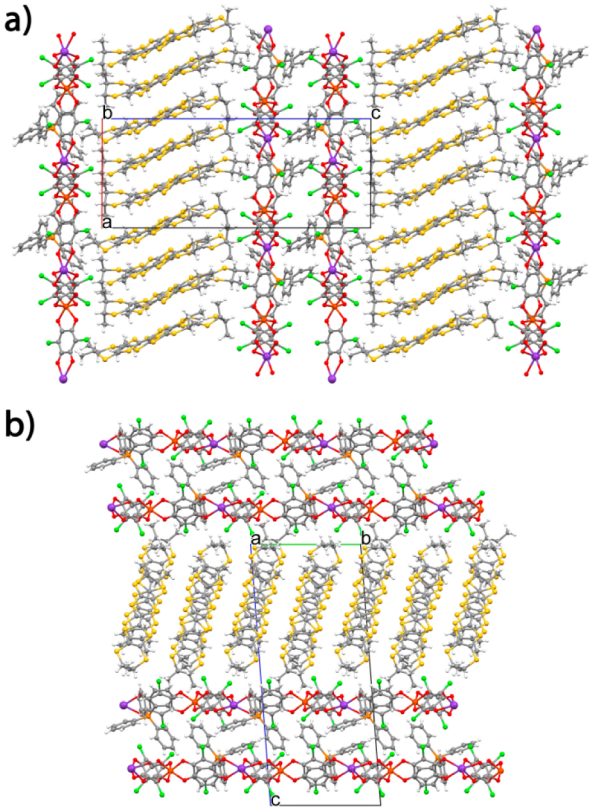

Figure 4. Crystal packing of **2** (a) in the *ac* plane, (b) in the *bc* plane, showing the organic−inorganic layer segregation. Crystallization water molecules were omitted for clarity.

TM-BEDT-TTF ((*S,S,S,S*)-enantiomer for **1**, (*R,R,R,R*)-enantiomer for **2**, and their racemic mixture for **3**) (Figure 4).

The organic layer shows **A**−**F** donor molecules arranged in the classical *β*-phase packing motif,[29] alternating along *a* in a −**B**−**E**−**C**− and a −**A**−**D**−**F**− sequence (Figure 5).

The analysis of the S···S short contacts reveals that lateral interstack interactions between donor molecules (represented in light blue in Figure 5) in the 3.41−3.66 Å range, are, on average, shorter than the intrastack ones, of 3.57−3.62 Å (represented in blue in Figure 5). Note that no S···S distances lower than the sum of the van der Waals radii (ca. 3.70 Å) are observed between **BC** and **AF** molecules (3.90−4.03 Å), so that the organic layer can be considered divided in three-molecule sublayers.

The analysis of the central C═C and internal C−S bond lengths for each crystallographically independent molecule for **2** (Table 3)[30] indicates that **B**, **D**, **E**, and **F** molecules bear a more positive charge than **A** and **C**, in agreement with their planar or bent shapes, respectively (Figure S4).

The structural features reported for **2** ((*R,R,R,R*)-enantiomer) are also valid for **1** ((*S,S,S,S*)-enantiomer) (Table S2) and **3** (racemic) (Table S3). The only difference for the racemic system **3**, when compared to **1** and **2**, consists in the presence of an −**A**−**C**−**B**− sequence of 2:1 alternate (*S,S,S,S*)-

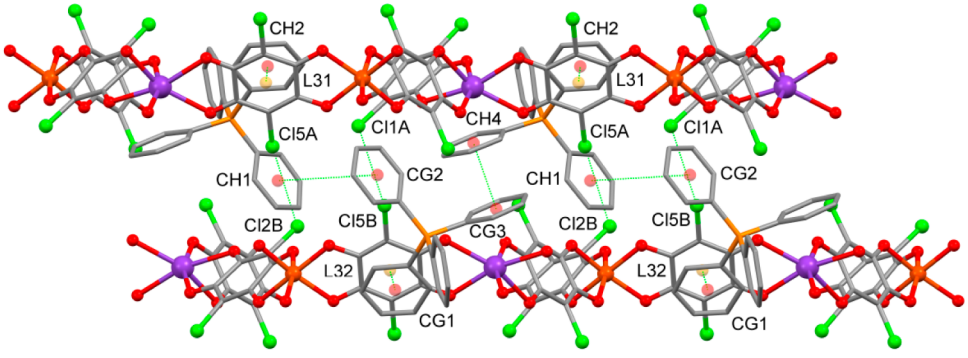

Figure 3. Side view of the inorganic anionic layers arranged in double-layers due to the establishment of intermolecular noncovalent interactions. Selected short contacts (Å): Cl(5A)···Cl(2B) 3.42, Cl(1A)···Cl(5B) 3.42, CH1···CG2 4.54, CH4···CG3 6.24, L31···CH2 4.00, L32···CG1 3.85. Legend: CH1, CH2, CG1, CG2 indicate calculated centroids on phenyl rings CXH1, CXH2, CXG1, CXG2 (X = 1−6), respectively; L31, L32 indicate calculated centroids on chloranilate rings CX31 and CX32 (X = 1−6), respectively.

DOI: 10.1021/acs.inorgchem.5b00261
Inorg. Chem. 2015, 54, 3643−3653

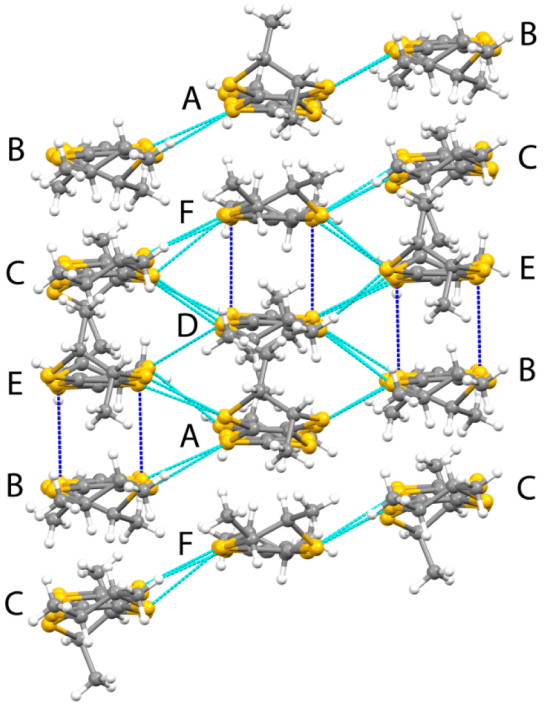

Figure 5. View of the TM-BEDT-TTF packing of **2** along the *ab* plane where the short intermolecular S···S contacts are highlighted. Some short contacts (Å): S(3F)···S(5D) 3.57, S(4F)···S(6D) 3.62, S(3E)···S(5B) 3.58, S(4E)···S(6B) 3.57, S(1F)···S(4C) 3.67, S(4C)···S(3F) 3.66, S(1D)···S(2C) 3.55, S(2C)···S(3D) 3.52, S(7F)···S(8C) 3.66, S(8D)···S(7D) 3.48, S(7D)···S(2E) 3.65, S(1B)···S(2D) 3.44, S(7E)···S(8F) 3.41.

and (*R,R,R,R*)-TM-BEDT-TTF donors in the organic layer (Figure S5). The S···S interstack (3.40−3.66 Å) and intrastack (3.59−3.60 Å) contacts (represented in light blue and blue, respectively, in Figure S5) have similar values to those of **1** and **2**.

Interestingly, the pairs of molecules where no S···S distances shorter than the sum of the van der Waals radii were observed (i.e., **BC** and **AF**) always involve a less positively charged molecule (**A** or **C**) (Figure 5). This can be likely responsible for the weaker intermolecular interactions observed between such sublayers.

It is noteworthy that the TM-BEDT-TTF organic donor in compounds **1**−**3** adopts two different conformations in the crystal packing. Two donor molecules per formula unit show the usual all-equatorial (eq) conformation for the four terminal methyl groups (Figure 6), encountered in most of the radical

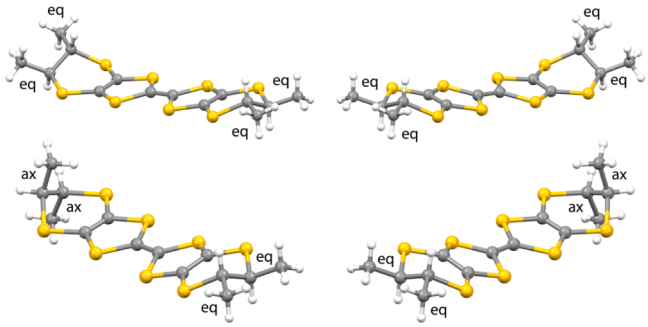

Figure 6. Molecular structure of the TM-BEDT-TTF organic donor in the all-eq conformation (top left (*S,S,S,S*) enantiomer, top right (*R,R,R,R*) enantiomer) and in the mixed (ax,ax,eq,eq) conformation (bottom left (*S,S,S,S*) enantiomer, bottom right (*R,R,R,R*) enantiomer).

cation salts of this donor,[11b,12,13,31] and also in its neutral form,[13] although this conformer is slightly less stable in the gas phase than the all-axial (ax) one.[13] Note that the later was also described in the solid state.[12] The other four donor molecules per formula unit in **1**−**3** present, instead, an unusual mixed conformation where the methyl groups adopt eq orientations on one ethylene bridge but ax orientations on the other ethylene bridge (Figure 6).

This (ax,ax,eq,eq) mixed conformation of TM-BEDT-TTF has been recently observed for charge transfer salts of the (*S,S,S,S*)-enantiomer with TCNQ[12] and also in a 1:1 cyclo-adduct of TM-BEDT-TTF with tetrachlorocatecholate.[32]

Finally, it should be pointed out which interactions are involved between the inorganic and organic layers. The position of the TM-BEDT-TTF donor molecules in the organic layers with respect to the vertexes of the hexagons occupied by alternate Fe^{III}/K^{I} metal centers is strongly determined by the hexagonal symmetry of the honeycomb inorganic layers (Figure 7 and S4).

For each pair of hexagons encompassing the organic layers, six donor molecules showing (ax,ax,eq,eq) conformation

Table 3. Bond Distance Analysis and Selected Bond Distances (Å) for the TM-BEDT-TTF Donor Molecules in 2

		A	B	C	D	E	F
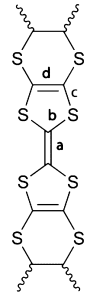	**a**	1.340(12)	1.343(12)	1.338(13)	1.354(11)	1.362(11)	1.372(12)
	b	1.758(9)	1.767(8)	1.761(9)	1.748(8)	1.740(8)	1.732(9)
		1.747(8)	1.741(8)	1.753(9)	1.752(8)	1.754(8)	1.765(8)
		1.772(7)	1.737(8)	1.760(7)	1.731(8)	1.763(8)	1.775(9)
		1.769(8)	1.761(9)	1.760(8)	1.762(8)	1.741(7)	1.699(9)
	c	1.749(8)	1.736(9)	1.762(9)	1.751(9)	1.763(8)	1.756(9)
		1.764(9)	1.777(8)	1.755(9)	1.790(8)	1.761(9)	1.757(9)
		1.772(7)	1.737(8)	1.760(7)	1.731(8)	1.763(8)	1.738(8)
		1.769(8)	1.761(9)	1.760(8)	1.762(8)	1.741(7)	1.743(8)
	d	1.392(11)	1.379(12)	1.363(11)	1.356(12)	1.334(11)	1.374(11)
		1.344(12)	1.358(11)	1.312(12)	1.370(10)	1.342(10)	1.363(12)
$\delta = (\mathbf{b}+\mathbf{c})-(\mathbf{a}+\mathbf{d})$	δ	0.817	0.793	0.807	0.790	0.798	0.751
$Q = 6.347-7.4638\cdot\delta$	Q	0.2(1)	0.4(1)	0.3(1)	0.4(1)	0.4(1)	0.7(1)

Q = calculated charge per donor.

DOI: 10.1021/acs.inorgchem.5b00261
Inorg. Chem. 2015, 54, 3643−3653

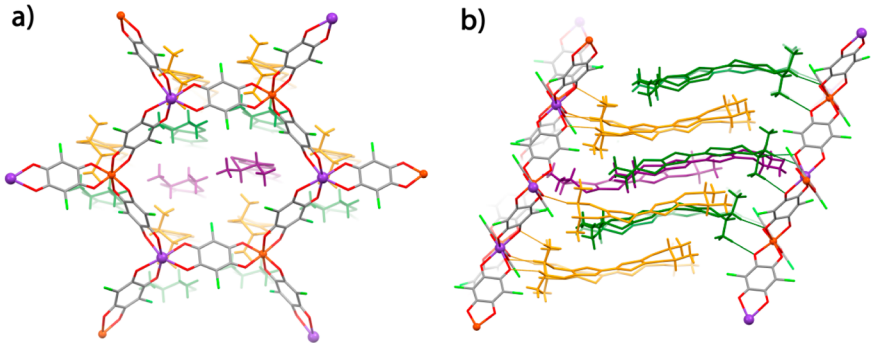

Figure 7. (a) Top view of the anionic layers parallel to the *ab* plane showing the specific position of the TM-BEDT-TTF organic donors with respect to the vertexes of the hexagons occupied by alternate metal centers; (b) Side view of the layers showing the short C−H···O contacts.

(represented in yellow in Figure 7) interact with the coordinated oxygen atoms of the same inorganic layer through short C−H···O contacts (2.20−2.66 Å), involving their axial methyl groups and the equatorial C−H of the ethylene bridge (Figure 7). Other six donor molecules having the same conformation (represented in green in Figure 7) interact, in the same way, with oxygen atoms of the inorganic layer located on the other side of the organic layer (Figure 7). Two donor molecules having the all-eq conformation (represented in purple in Figure 7) occupy, instead, the center of the hexagon without interacting with the complexes. Thus, it is clear that the chloranilate-based honeycomb layers strongly influence the disposition and conformation of the organic donors in the crystal structure, which, in turn, ultimately influence the resulting physical properties.

Transport Properties and Band Structure Calculations. The two-point conductivity measurements for compounds **1** and **3** show room-temperature conductivity values of ca. 3×10^{-4} S cm^{-1} that decrease in a semiconducting way as the samples are cooled (Figure 8). The Arrhenius plot, $\ln(\sigma)$ vs

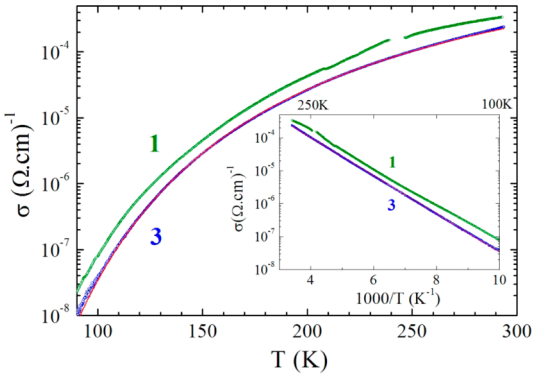

Figure 8. Thermal variation of the electrical conductivity for compounds **1** and **3**. The inset shows the Arrhenius plot. The red line is the Arrhenius fit to the data for compound **3**.

$1/T$ (inset of Figure 8) shows a linear behavior that can be fitted to the law $\ln(\sigma) = \ln(\sigma_0) - E_a/k_BT$ with an activation energy E_a of ca. 1300−1400 K corresponding to ca. 110−120 meV.

This behavior indicates that compounds **1**−**3** are semiconductors with low room-temperature conductivity and a medium value of activation energy. No significant difference between the enantiopure and the racemic systems is observed. These results are in agreement with the structural data showing the presence of a neutral TM-BEDT-TTF molecule out of three in the crystal packing, thus precluding an efficient charge delocalization along the organic layers, and also with the band structure calculations (*vide infra*).

In order to get insight on the origin of the activated conductivity of these systems, band structure calculations were performed on compound **1**. The repeating unit of the donor layers contains six symmetry nonequivalent donors with an average charge of +1/3. Consequently, the calculated band structure near the Fermi level for this salt contains six bands mostly based on the HOMOs of the different TM-BEDT-TTF donors (Figure 9). Because of the stoichiometry, these bands

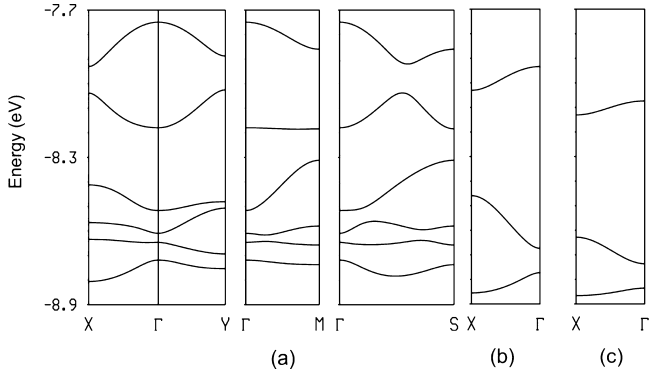

Figure 9. Electronic structure for **1**. Calculated band structure of the following: (a) the $[(\text{TM-BEDT-TTF})_6]^{2+}$ donor layers, (b) the isolated **−B−E−C−** chains, and (c) the isolated **−A−D−F−** chains, where Γ = (0, 0), X = (a*/2, 0), Y = (0, b*/2), M = (a*/2, b*/2) and S = (−a*/2, b*/2).

must contain two holes so that the equivalent of one of these bands must be empty. Because there is a band gap separating the upper band from the lower ones, the upper band is completely empty. This salt is thus predicted to be a regular (band gap) semiconductor in agreement with the transport measurements.

What is the origin of the activated conductivity of this salt? The donor layers can be described as a series of parallel stacks along the *a*-direction; they contain six different donors (labeled **A**, **B**, ..., **F**), and there are 18 different types of interactions between the HOMOs of these molecules (labeled I, II, ..., XVIII) (Figure 10). The HOMO energies of the six donors are found within a relatively broad energy range: −8.806 eV (**A**), −8.698 eV (**C**), −8.660 eV (**D**), −8.528 eV (**E**), −8.514 eV (**F**) and −8.478 eV (**B**). There are three donors (**B**, **E** and **F**) with relatively high energy HOMOs but only two holes to be placed

DOI: 10.1021/acs.inorgchem.5b00261
Inorg. Chem. 2015, 54, 3643−3653

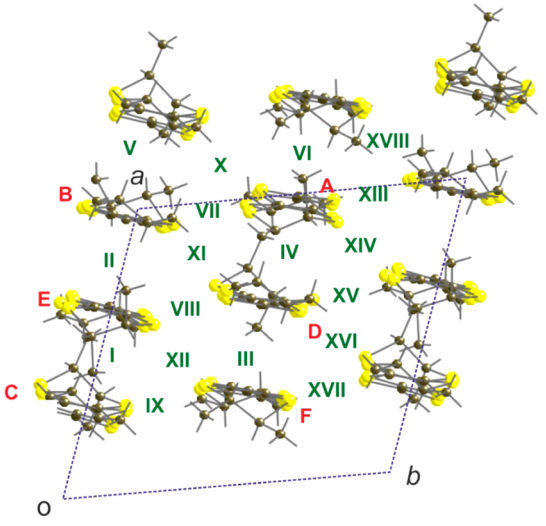

Figure 10. Donor layer of **1** where the six different donors and 18 different HOMO···HOMO interactions are shown.

in the upper HOMO band. It is thus not clear where these holes are located, so that they will be most likely delocalized.

In understanding this question it is essential to have an idea of the strength of the different HOMO···HOMO interactions in the donor layers. The 18 interactions in Figure 10 can be classified into three different classes: (a) interactions within the stacks along the *a*-direction (I, II, ...,VI), (b) lateral interactions along the *b*-direction (VII, VIII, IX, XIII, XV, and XVII), mostly of π-type, and (c) interactions along the step-chains **−B−D−C−A−E−F−** (X, XI, XII, XIV, XVI, and XVIII). The strength of these HOMO···HOMO interactions may be quantified from the absolute value of the HOMO···HOMO interaction energy, $|\beta_{HOMO-HOMO}|$, associated with each interaction.[33] The calculated values for the 18 interactions are reported in Table 4.

Table 4. $|\beta_{HOMO-HOMO}|$ Interaction Energies (eV) for the Donor···Donor Interactions Defined in Figure 10

interaction		$\lvert\beta_{HOMO-HOMO}\rvert$	interaction		$\lvert\beta_{HOMO-HOMO}\rvert$
I	(E−C)	0.2178	II	(E−B)	0.5355
III	(D−F)	0.4783	IV	(A−D)	0.1231
V	(B−C)	0.3684	VI	(A−F)	0.3054
VII	(B−A)	0.0022	VIII	(E−D)	0.0138
IX	(C−F)	0.0028	X	(A−C)	0.0918
XI	(B−D)	0.1163	XII	(E−F)	0.0910
XIII	(A−B)	0.0004	XIV	(A−E)	0.0911
XV	(D−E)	0.0154	XVI	(D−C)	0.0714
XVII	(C−F)	0.0143	XVIII	(B−F)	0.0871

Consideration of these results leads to the following observations. First, the interactions along the stacks in the *a*-direction are by far the strongest ones. Second, the lateral π-type interactions along the *b*-direction are negligible. Third, the interactions along the step-chains are quite sizable even if weaker than those along the stacks. Consequently, as far as the HOMO···HOMO interactions are concerned, the donor layers of the present salt should be described as a series of substantially coupled parallel stacks along *a*.

Thus, a useful way to understand the electronic features of the donor layers is to consider the two different chains as the building blocks. The calculated band structures for the isolated **−B−E−C−** and **−A−D−F−** chains are shown in Figures 9b and 9c, respectively. In both cases, the upper band is strongly separated from the two lower ones. The upper, well-separated bands mostly originate from the antibonding combination of the HOMOs of donors **B** and **E** (Figure 9b) and the antibonding combination of the HOMOs of donors **D** and **F** (Figure 9c), because II (**B−E**) and III (**D−F**) are by far the strongest interactions within each chain. Because all interactions are stronger for the **−B−E−C−** chain, the upper band of this chain is the highest in energy. When the interactions along the step-chains are switched on, the bands of the isolated chains communicate and acquire additional dispersion both along the chain and interchain directions. However, the initial separation and the strength of the interactions are large enough to ensure that the two bands remain well separated all along the Brillouin zone. If the two chains had been more similar in terms of the strength of the HOMO···HOMO interactions, it is quite possible that a semimetallic-type overlap of the two bands had occurred and the conductivity could have been nonactivated.

With these results in mind, we have analyzed the composition of the upper empty band in Figure 9a. We have found that the upper band is delocalized among the two different chains though more strongly based on the **−B−E−C−** one: around three-quarters of the electron density associated with this band originates from the levels of the **−B−E−C−** chains and one-quarter from the levels of the **−A−D−F−** chains. However, the participation of the donors of a given chain is very different: 67% of the electron density originates from the **B−E** dimer, 7% from donor **C**, 23% from the **D−F** dimer, and 3% from donor **A**. Thus, two of the donors, **A** and **C**, have a very small participation in this band and can be considered as essentially neutral, in accordance with the structural findings. All these results are in agreement with the previous analysis. Thus, the picture emerging from this study is that the two holes in the band structure are delocalized among the antibonding combination of the HOMO levels of both the **B−E** and **D−F** dimers, which are coupled through the interactions along the step-chains (depicted in blue in Figure 5), although with a larger weight in the **B−E** dimers. The composition of the upper filled band in Figure 9a is the counterpart of the upper empty band; that is, it is delocalized between the antibonding combination of the HOMO levels of both the **B−E** and **D−F** dimers but with a larger weight on the **D-F** dimers.

The transport in an intrinsic semiconducting way is due to the holes created in the upper filled band and the electrons filling the lower empty band because of the thermal excitation. Thus, the conductivity carriers in this salt are both delocalized among the two types of dimers of the layer (though the holes and electrons are more strongly tight to the **D−F** and **B−E** dimers, respectively), whereas donors **A** and **C** practically do not contribute to the conductivity.

Given the similar conductivity behavior, electrical conductivity at room temperature, and activation energy values for the three components of this series, along with their isostructurality, the band structure calculation and the explanation of the origin of the activated conductivity for **1** can be reasonably extended to **2** and **3**.

Magnetic Measurements. The temperature dependence of the magnetic susceptibility for **3** is shown in Figure 11 as a χT versus T plot. The χT value at room temperature of ca. 4.4 cm^3 K mol^{-1} is close to the expected value (4.375 cm^3 K mol^{-1}) for isolated high spin Fe(III) centers ($S = 5/2$, $g = 2$) suggesting a negligible paramagnetic contribution from the

DOI: 10.1021/acs.inorgchem.5b00261
Inorg. Chem. 2015, 54, 3643−3653

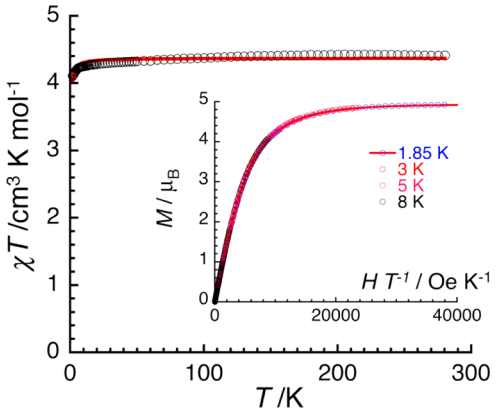

Figure 11. Temperature dependence of χT product at 1000 Oe (where χ is the molar magnetic susceptibility equal to the ratio between the magnetization and the applied magnetic field, M/H, per mole of Fe(III) complex) between 1.85 and 280 K for a polycrystalline sample of **3**. The solid line is the best fit obtained using a Curie−Weiss law. Inset: M vs H/T plot for **3** between 1.85 and 8 K at magnetic fields between 0 and 7 T. The solid line is the best fit obtained using S = 5/2 Brillouin function.

organic TM-BEDT-TTF molecules. This χT product remains constant down to ca. 20 K, then the χT product decreases slightly to 4.1 cm^3 K mol^{-1} at 1.85 K. The observed behavior is typical of magnetically isolated S = 5/2 ions with extremely small antiferromagnetic interactions between the isotropic Fe(III) magnetic sites. On the basis of the crystal structure (*vide supra*), which highlights the presence of Fe(III) ions connected through chloranilate bridging ligands but separated by diamagnetic K(I) ions, the magnetic data have been modeled in the frame of the mean-field approximation using the well-known Curie−Weiss law.

This model satisfactorily reproduces the magnetic properties of compound **3** in the whole temperature range, with g = 2.00(5) and zJ/k_B = −84(10) mK. The magnitude of the magnetic interactions falls well in the range expected for dipolar magnetic interactions. The field dependence of the magnetization below 8 K supports the S = 5/2 ground spin state of the Fe(III) ions for **3** because a Brillouin function for an S = 5/2 spin state reproduces well the experimental data with g = 2.00(2) (Inset in Figure 11). Thus, compound **3** exhibits a high spin configuration for the Fe(III) ions with an S = 5/2 ground spin state and shows a typical paramagnetic behavior of quasi-isolated ions, because the M···M distances between paramagnetic metal centers (ca. 13.6 Å through space and ca. 16.2 Å through the bridging ligands) are too large to allow significant magnetic interactions.

As far as the contribution of the TM-BEDT-TTF donors is concerned, the expected contribution of the paramagnetic radical cations is not observed in the χT versus T plot. A slight decrease of the χT value associated with the Fe(III) contribution is observed in the whole temperature range, indicating that the contribution of the donors seems mainly hidden. This is not surprising given the +1/2 charge of two out of three donor molecules per formula unit (i.e., half unpaired delocalized electron per partially oxidized donor molecule) when compared to the S = 5/2 contribution of the Fe(III) centers (i.e., five unpaired localized electrons per ion). However, the structural analysis reveals the presence of short contacts between pairs of charged donor molecules (**BE** and **DF**) (depicted in blue in Figure 5) that can be at the origin of an antiferromagnetic coupling. Therefore, it seems reasonable to consider the unpaired delocalized electrons of the organic donors as antiferromagnetically coupled in the whole temperature range, in order to explain their negligible contribution to the overall magnetic susceptibility of this system. The establishment of strong contacts between **BE** and **DF** molecules pairs is further confirmed by the band structure calculations that predict a partial degree of dimerization for the electrons of these molecules.

CONCLUSIONS

A complete series of isostructural crystalline mixed valence radical cation salts based on the TM-BEDT-TTF chiral donor and chloranilate-bridged heterobimetallic honeycomb layers were prepared via electrocrystallization. The use of the "complex as ligand" approach during the electrocrystallization experiments has been successful for obtaining these systems where the self-assembling of the tris(chloranilato)ferrate(III) anion with potassium cations afforded anionic layers, that further template the structure in segregated organic and inorganic layers. As a common structural feature for the three systems, one can disclose the presence of inorganic layers associated in double-layers, as a result of two major intermolecular interactions, Cl···Cl and $\pi-\pi$ stacking, between the chloranilate ligands and the PPh_4^+ charge-compensating cations, and the simultaneous presence of two different conformations of the TM-BEDT-TTF donor in the crystal packing, very likely due to the diverse interactions of the terminal methyl groups with the oxygen atoms of the chloranilate ligands. The structural analyses and band structure calculations are in agreement with the single crystal conductivity measurements showing semiconducting behavior for the three materials, with low room-temperature conductivity and a medium value for the activation energy, as expected from the presence of one neutral TM-BEDT-TTF donor in the crystal packing and the presence of a slight dimerization between the partially oxidized molecules. Magnetic susceptibility measurements for **3** indicate the presence of quasi-isolated high spin S = 5/2 Fe(III) ions, with a negligible contribution from the TM-BEDT-TTF radical cations. This first family of isostructural chiral conducting radical cation salts based on magnetic chloranilate-bridged heterobimetallic honeycomb layers demonstrates the versatility of these anions for the preparation of $\pi-d$ multifunctional molecular materials where properties such as charge transport, magnetism, and chirality coexist in the same crystal lattice. Moreover, a deep knowledge of the structure/properties relationship in these materials is of fundamental importance for a rational design of chiral conductors showing the eMChA effect as a synergy between chirality and conductivity.

EXPERIMENTAL SECTION

General. $[PPh_4]_3[Fe(Cl_2An)_3]$,[21] (*S,S,S,S*)-TM-BEDT-TTF and (*R,R,R,R*)-TM-BEDT-TTF[13] were synthesized according to the literature procedures. Crystals were grown by the electrocrystallization technique.[34] Solvents used for electrocrystallization experiments (HPLC grade) were dried under basic alumina and degassed with argon prior to use.

Syntheses. *β-[(S,S,S,S)-TM-BEDT-TTF]$_3$PPh$_4$[K^{I}Fe^{III}(Cl$_2$An)$_3$]·3H$_2$O* (***1***). $[PPh_4]_3[Fe(Cl_2An)_3]$ (8 mg) was dissolved in 7 mL of CH_3CN and placed in the cathode chamber of an H-shape electrocrystallization cell together with 2 mg of KCl. (*S,S,S,S*)-

DOI: 10.1021/acs.inorgchem.5b00261
Inorg. Chem. 2015, 54, 3643−3653

Table 5. Summary of X-ray Crystallographic Data for 1, 2, and 3

	1	2	3
empirical formula	$C_{168}H_{136}Cl_{12}Fe_2K_2O_{30}P_2S_{48}$	$C_{168}H_{136}Cl_{12}Fe_2K_2O_{30}P_2S_{48}$	$C_{84}H_{68}Cl_6FeKO_{15}PS_{24}$
fw	4850.89	4850.89	2417.44
cryst size, mm	0.50 × 0.27 × 0.04	0.60 × 0.60 × 0.40	0.11 × 0.06 × 0.02
cryst syst	triclinic	triclinic	triclinic
space group	*P*1	*P*1	*P*−1
a, Å	13.629(1)	13.635(1)	13.598(3)
b, Å	14.174(2)	14.148(2)	14.171(2)
c, Å	30.143(8)	30.122(5)	30.107(7)
α, deg	85.370(15)	85.210(13)	85.659(12)
β, deg	88.106(10)	88.033(10)	88.219(17)
γ, deg	63.346(9)	63.419(8)	63.378(12)
V, Å^3	5187(1)	5178(1)	5172(2)
Z	1	1	2
T, K	150(2)	150(2)	150(2)
ρ (calc), Mg/m^3	1.553	1.556	1.552
μ, mm^{-1}	0.898	0.899	0.900
θ range, deg	1.61−26.00	1.61−27.50	1.61−25.25
GOF	1.005	1.032	1.000
Flack parameter	0.15(4)	0.09(3)	−
*R*1[a]	0.0883	0.0742	0.1078
*wR*2[a]	0.2118	0.1904	0.2531

[a] $R1 = \Sigma||F_o| - |F_c||/\Sigma|F_o|$, $wR2 = [\Sigma[w(F_o^2 - F_c^2)^2]/\Sigma[w(F_o^2)^2]]^{1/2}$, $w = 1/[\sigma^2(F_o^2) + (aP)^2 + bP]$, where $P = [\max(F_o^2,0) + 2F_c^2]/3$.

TM-BEDT-TTF (3 mg) was dissolved in 7 mL of CH_3CN and placed in the anode chamber of the cell. A current density of 1.0 μA cm^{-2} was applied. Black prismatic single crystals of **1** were grown at 20 °C on the anode surface of a platinum wire electrode over 2 weeks.

β-[(R,R,R,R)-TM-BEDT-TTF]$_3$PPh$_4$[K^{I}Fe^{III}(Cl$_2$An)$_3$]·3H$_2$O (**2**). $[PPh_4]_3[Fe(Cl_2An)_3]$ (8 mg) was dissolved in 7 mL of CH_3CN and placed in the cathode chamber of an H-shape electrocrystallization cell together with 2 mg of KCl. (*R,R,R,R*)-TM-BEDT-TTF (3 mg) was dissolved in 7 mL of CH_3CN and placed in the anode chamber of the cell. A current density of 1.0 μA cm^{-2} was applied. Black prismatic single crystals of **2** were grown at 20 °C on the anode surface of a platinum wire electrode over 2 weeks.

β-[(rac)-TM-BEDT-TTF]$_3$PPh$_4$[K^{I}Fe^{III}(Cl$_2$An)$_3$]·3H$_2$O (**3**). $[PPh_4]_3[Fe(Cl_2An)_3]$ (8 mg) was dissolved in 7 mL of CH_3CN and placed in the cathode chamber of an H-shape electrocrystallization cell together with 2 mg of KCl. (*rac*)-TM-BEDT-TTF (3 mg), obtained by mixing 1.5 mg of (*S,S,S,S*)-TM-BEDT-TTF and 1.5 mg of (*R,R,R,R*)-TM-BEDT-TTF, was dissolved in 7 mL of CH_3CN and placed in the anode chamber of the cell. A current density of 1.0 μA cm^{-2} was applied. Black elongated prismatic single crystals of **3** were grown at 20 °C on the anode surface of a platinum wire electrode over 1 week.

X-ray Crystallography. X-ray diffraction measurements were performed on a Bruker Nonius Kappa CCD diffractometer, using graphite-monochromated Mo K*α* radiation (*λ* = 0.71073 Å). The structures were solved by direct methods (SHELXS-97) and refined on F^2 with full-matrix least-squares (SHELXL-97),[35] using the Wingx software package.[36] The non-H atoms were refined with anisotropic displacement parameters. The crystallization water molecules were refined without the hydrogen atoms. A summary of the crystallographic data and the structure refinement for **1**−**3** is reported in Table 5. Crystallographic data for the structures have been deposited in the Cambridge Crystallographic Data Centre (see Supporting Information).

Single Crystal Conductivity Measurements. Electrical transport measurements were performed on platelet-shaped single crystals. Gold contacts were evaporated on both faces of the crystals and gold wires (17 μm diameter) were glued with silver paste on those contacts. Two-probe DC measurements were performed applying a constant voltage in the range 0.5−1 V and measuring the current using a Keithley 6487 Picoammeter/Voltage Source. Low temperature was provided by a homemade cryostat equipped with a 4 K pulse-tube.

Band Structure Calculations. The tight-binding band structure calculations were of the extended Hückel type.[37] A modified Wolfsberg−Helmholtz formula was used to calculate the nondiagonal $H_{\mu\nu}$ values.[38] All valence electrons were taken into account in the calculations and the basis set consisted of Slater-type orbitals of double-*ζ* quality for C 2s and 2p, S 3s and 3p, and of single-*ζ* quality for H. The ionization potentials, contraction coefficients, and exponents were taken from previous work.[39]

Magnetic Measurements. The magnetic susceptibility measurements were performed with a MPMS-XL Quantum Design SQUID magnetometer that works between 1.8 and 400 K for dc applied fields ranging from −7 to +7 T. Measurements were performed on a polycrystalline sample of 3.6 mg for **3**, introduced in a polyethylene sample holder (3 × 0.5 × 0.02 cm). *M* vs *H* measurements have been performed at 100 K to check for the presence of ferromagnetic impurities that has been found absent. The magnetic data were corrected for the sample holder and the diamagnetic contribution (−1.5 × 10^{-3} cm^3/mol for **3** that compares well with the expected theoretical value of −1.2 × 10^{-3} cm^3/mol from −Mw/2 × 10^{-6} cm^3/mol).

■ ASSOCIATED CONTENT

Ⓢ Supporting Information

X-ray crystallographic files in CIF format, additional figures and tables as mentioned in the text. This material is available free of charge via the Internet at http://pubs.acs.org. Crystallographic data for the structures have been deposited in the Cambridge

DOI: 10.1021/acs.inorgchem.5b00261
Inorg. Chem. 2015, 54, 3643−3653

Crystallographic Data Centre, deposition numbers CCDC 1047177 (**1**), CCDC 1047178 (**2**), CCDC 1047179 (**3**). These data can be obtained free of charge from The Cambridge Crystallographic Data Centre via www.ccdc.cam.ac.uk/data_request/cif.

AUTHOR INFORMATION

Corresponding Authors

*E-mail: mercuri@unica.it. Fax: (+39) 070 675 4486. Tel: (+39) 070 675 4486.

*E-mail: narcis.avarvari@univ-angers.fr. Fax: (+33) 02 41 73 54 05. Tel: (+33) 02 41 73 50 84.

Notes

The authors declare no competing financial interest.

ACKNOWLEDGMENTS

This work was supported in France by the CNRS, the University of Angers, the University of Bordeaux, the Aquitaine Region, and the National Agency for Research (ANR) (ANR Inter, ANR-12-IS07-0004-04, CREMM project). The work in Italy was supported by Regione Autonoma della Sardegna, L.R. 7-8-2007, Bando 2009, CRP-17453 Project "Nano Materiali Multifunzionali per Applicazioni nell'Elettronica Molecolare", Fondazione Banco di Sardegna and INSTM. Work at Bellaterra was supported by a MINECO-Spain (Grant FIS2012-37549-C05-05) and Generalitat de Catalunya (2014SGR301)

REFERENCES

(1) Avarvari, N.; Wallis, J. D. *J. Mater. Chem.* **2009**, *19*, 4061−4076.

(2) (a) Coronado, E.; Day, P. *Chem. Rev.* **2004**, *104*, 5419−5448. (b) Coronado, E.; Galán-Mascarós, J. R. *J. Mater. Chem.* **2005**, *15*, 66−74. (c) Lorcy, D.; Bellec, N.; Fourmigué, M.; Avarvari, N. *Coord. Chem. Rev.* **2009**, *253*, 1398−1438.

(3) Pop, F.; Auban-Senzier, P.; Canadell, E.; Rikken, G. L. J. A.; Avarvari, N. *Nat. Commun.* **2014**, *5*, 3757 DOI: 10.1038/ncomms4757.

(4) (a) Rikken, G. L. J. A.; Fölling, J.; Wyder, P. *Phys. Rev. Lett.* **2001**, *87*, 236602-1−236602-4. (b) Krstić, V.; Roth, S.; Burghard, M.; Kern, K.; Rikken, G. L. J. A. *J. Chem. Phys.* **2002**, *117*, 11315−11319. (c) De Martino, A.; Egger, R.; Tsvelik, A. M. *Phys. Rev. Lett.* **2006**, *97*, 076402-1−076402-4.

(5) (a) Réthoré, C.; Fourmigué, M.; Avarvari, N. *Chem. Commun.* **2004**, 1384−1385. (b) Réthoré, C.; Avarvari, N.; Canadell, E.; Auban-Senzier, P.; Fourmigué, M. *J. Am. Chem. Soc.* **2005**, *127*, 5748−5749. (c) Madalan, A. M.; Réthoré, C.; Fourmigué, M.; Canadell, E.; Lopes, E. B.; Almeida, M.; Auban-Senzier, P.; Avarvari, N. *Chem.—Eur. J.* **2010**, *16*, 528−537. (d) Olejniczak, I.; Frąckowiak, A.; Matysiak, J.; Madalan, A.; Pop, F.; Avarvari, N. *Cent. Eur. J. Phys.* **2014**, *12*, 215−220.

(6) Hasegawa, M.; Sone, Y.; Iwata, S.; Matsuzawa, H.; Mazaki, Y. *Org. Lett.* **2011**, *13*, 4688−4691.

(7) Biet, T.; Fihey, A.; Cauchy, T.; Vanthuyne, N.; Roussel, C.; Crassous, J.; Avarvari, N. *Chem.—Eur. J.* **2013**, *19*, 13160−13167.

(8) (a) Danila, I.; Riobé, F.; Puigmartí-Luis, J.; Pérez del Pino, Á.; Wallis, J. D.; Amabilino, D. B.; Avarvari, N. *J. Mater. Chem.* **2009**, *19*, 4495−4504. (b) Danila, I.; Riobé, F.; Piron, F.; Puigmartí-Luis, J.; Wallis, J. D.; Linares, M.; Ågren, H.; Beljonne, D.; Amabilino, D. B.; Avarvari, N. *J. Am. Chem. Soc.* **2011**, *133*, 8344−8353. (c) Danila, I.; Pop, F.; Escudero, C.; Feldborg, L. N.; Puigmartí-Luis, J.; Riobé, F.; Avarvari, N.; Amabilino, D. B. *Chem. Commun.* **2012**, *48*, 4552−4554. (d) Pop, F.; Melan, C.; Danila, I.; Linares, M.; Beljonne, D.; Amabilino, D. B.; N. Avarvari, N. *Chem.—Eur. J.* **2014**, *20*, 17443−17453.

(9) Pop, F.; Auban-Senzier, P.; Frąckowiak, A.; Ptaszyński, K.; Olejniczak, I.; Wallis, J. D.; Canadell, E.; Avarvari, N. *J. Am. Chem. Soc.* **2013**, *135*, 17176−17186.

(10) (a) Madalan, A. M.; Réthoré, C.; Avarvari, N. *Inorg. Chim. Acta* **2007**, *360*, 233−240. (b) Riobé, F.; Avarvari, N. *Chem. Commun.* **2009**, 3753−3755. (c) Riobé, F.; Avarvari, N. *Coord. Chem. Rev.* **2010**, *254*, 1523−1533.

(11) (a) Dunitz, J. D.; Karrer, A.; Wallis, J. D. *Helv. Chim. Acta* **1986**, *69*, 69−70. (b) Karrer, A.; Wallis, J. D.; Dunitz, J. D.; Hilti, B.; Mayer, C. W.; Bürkle, M.; Pfeiffer, J. *Helv. Chim. Acta* **1987**, *70*, 942−953.

(12) Yang, S.; Pop, F.; Melan, C.; Brooks, A. C.; Martin, L.; Horton, P.; Auban-Senzier, P.; Rikken, G. L. J. A.; Avarvari, N.; Wallis, J. D. *CrystEngComm* **2014**, *16*, 3906−3916.

(13) Pop, F.; Laroussi, S.; Cauchy, T.; Gómez-García, C. J.; Wallis, J. D.; Avarvari, N. *Chirality* **2013**, *25*, 466−474.

(14) Galán-Mascarós, J. R.; Coronado, E.; Goddard, P. A.; Singleton, J.; Coldea, A. I.; Wallis, J. D.; Coles, S. J.; Alberola, A. *J. Am. Chem. Soc.* **2010**, *132*, 9271−9273.

(15) (a) Coronado, E.; Day, P. *Chem. Rev.* **2004**, *104*, 5419−5448. (b) Coronado, E.; Galán-Mascarós, J. R. *J. Mater. Chem.* **2005**, *15*, 66−74. (c) Martin, L.; Day, P.; Akutsu, H.; Yamada, J.; Nakatsuji, S.; Clegg, W.; Harrington, R. W.; Horton, P. N.; Hursthouse, M. B.; McMillan, P.; Firth, S. *CrystEngComm.* **2007**, *9*, 865−867.

(16) (a) Gómez-García, C. J.; Coronado, E.; Curreli, S.; Giménez-Saiz, C.; Deplano, P.; Mercuri, M. L.; Pilia, L.; Serpe, A.; Faulmann, C.; Canadell, E. *Chem. Commun.* **2006**, 4931−4933. (b) Coronado, E.; Curreli, S.; Giménez-Saiz, C.; Gómez-García, C. J.; Deplano, P.; Mercuri, M. L.; Serpe, A.; Pilia, L.; Faulmann, C.; Canadell, E. *Inorg. Chem.* **2007**, *46*, 4446−4457.

(17) Madalan, A. M.; Canadell, E.; Auban-Senzier, P.; Brânzea, D.; Avarvari, N.; Andruh, M. *New J. Chem.* **2008**, *32*, 333−339.

(18) Martin, L.; Day, P.; Horton, P.; Nakatsuji, S.; Yamada, J.; Akutsu, H. *J. Mater. Chem.* **2010**, *20*, 2738−2742.

(19) Pop, F.; Allain, M.; Auban-Senzier, P.; Martínez-Lillo, J.; Lloret, F.; Julve, M.; Canadell, E.; Avarvari, N. *Eur. J. Inorg. Chem.* **2014**, 3855−3862.

(20) Atzori, M.; Marchiò, L.; Clérac, R.; Serpe, A.; Deplano, P.; Avarvari, N.; Mercuri, M. L. *Cryst. Growth Des.* **2014**, *14*, 5938−5948.

(21) Atzori, M.; Artizzu, F.; Sessini, E.; Marchiò, L.; Loche, D.; Serpe, A.; Deplano, P.; Concas, G.; Pop, F.; Avarvari, N.; Mercuri, M. L. *Dalton Trans.* **2014**, *43*, 7006−7019.

(22) Atzori, M.; Pop, F.; Auban-Senzier, P.; Gómez-García, C. J.; Canadell, E.; Artizzu, F.; Serpe, A.; Deplano, P.; Avarvari, N.; Mercuri, M. L. *Inorg. Chem.* **2014**, *53*, 7028−7039.

(23) Atzori, M.; Benmansour, S.; Mínguez Espallargas, G.; Clemente-León, M.; Abhervé, A.; Gómez-Claramunt, P.; Coronado, E.; Artizzu, F.; Sessini, E.; Deplano, P.; Serpe, A.; Mercuri, M. L.; Gómez García, C. J. *Inorg. Chem.* **2013**, *52*, 10031−10040.

(24) Atzori, M.; Pop, F.; Cauchy, T.; Mercuri, M. L.; Avarvari, N. *Org. Biomol. Chem.* **2014**, *12*, 8752−8763.

(25) Mouchaham, G.; Roques, N.; Duhayon, C.; Imaz, I.; Sutter, J.-P. *New J. Chem.* **2013**, *37*, 3476−3487.

(26) Molčanov, K.; Kojić-Prodić, B.; Meden, A. *CrystEngComm* **2009**, *11*, 1407−1415.

(27) Abrahams, B. F.; Grannas, M. J.; Hudson, T. A.; Hughes, S. A.; Pranoto, N. H.; Robson, R. *Dalton Trans.* **2011**, *40*, 12242−12247.

(28) Luo, T.-T.; Liu, Y.-H.; Tsai, H.-L.; Su, C.-C.; Ueng, C.-H.; Lu, K.-L. *Eur. J. Inorg. Chem.* **2004**, 4253−4258.

(29) Mori, T. *Bull. Chem. Soc. Jpn.* **1998**, *71*, 2509−2526.

(30) Guionneau, P.; Kepert, C. J.; Bravic, G.; Chasseau, D.; Truter, M. R.; Kurmoo, M.; Day, P. *Synth. Met.* **1997**, *86*, 1973−1974.

(31) Riobé, F.; Piron, F.; Réthoré, C.; Madalan, A. M.; Gómez-García, C. J.; Lacour, J.; Wallis, J. D.; Avarvari, N. *New J. Chem.* **2011**, *35*, 2279−2286.

(32) Pop, F.; Lacour, J.; Avarvari, N. *Rev. Roum. Ch.* **2012**, *57*, 457−462.

(33) Whangbo, M.-H.; Williams, J. M.; Leung, P. C. W.; Beno, M. A.; Emge, T. J.; Wang, H. H. *Inorg. Chem.* **1985**, *24*, 3500−3502.

(34) (a) Emge, T. J.; Wang, H. H.; Beno, M. A.; Williams, J. M.; Whangbo, M. H.; Evain, M. *J. Am. Chem. Soc.* **1986**, *108*, 8215−8223. (b) Stephens, D. A.; Rehan, A. E.; Compton, S. J.; Barkhau, R. A.; Williams, J. M. *Inorg. Synth.* **1986**, *24*, 130−143. (c) Batail, P.;

DOI: 10.1021/acs.inorgchem.5b00261
Inorg. Chem. 2015, 54, 3643−3653

Boubekeur, K.; Fourmigué, M.; Gabriel, J.-C. P. *Chem. Mater.* **1998**, *10*, 3005−3015.
(35) Sheldrick, G. M. *Programs for the Refinement of Crystal Structures*; University of Göttingen: Göttingen, Germany, 1996.
(36) Farrugia, L. J. *J. Appl. Crystallogr.* **1999**, *32*, 837−838.
(37) Whangbo, M.-H.; Hoffmann, R. *J. Am. Chem. Soc.* **1978**, *100*, 6093−6098.
(38) Ammeter, J. H.; Bürgi, H.-B.; Thibeault, J.; Hoffmann, R. *J. Am. Chem. Soc.* **1978**, *100*, 3686−3692.
(39) Pénicaud, A.; Boubekeur, K.; Batail, P.; Canadell, E.; Auban-Senzier, P.; Jérome, D. *J. Am. Chem. Soc.* **1993**, *115*, 4101−4112.

DOI: 10.1021/acs.inorgchem.5b00261
Inorg. Chem. 2015, 54, 3643−3653